PREDICTION OF FLIGHT MEASUREMENTS OF HIGH ENTHALPY NONEQUILIBRIUM FLOW FROM A CUBESAT-CLASS ATMOSPHERIC PROBE

BY

JONATHAN MORGAN

THESIS

Submitted in partial fulfillment of the requirements
for the degree of Master of Science in Aerospace Engineering
in the Graduate College of the
University of Illinois at Urbana-Champaign, 2018

Urbana, Illinois

Advisor:
Professor Deborah Levin

Abstract

Spectral radiation is sensitive to many physical chemical aspects of high-enthalpy, non-equilibrium flows affect radiation and heat transfer estimates at low-earth altitudes, which is important as a flow diagnostic. For diatomic molecules, high energy collisions in the bow shock region result in ro-vibrionic transitions and release of photons in different wavelength bands. In this work, the Direct Simulations Monte Carlo (DSMC) method is used for the SASSI^2 mission to determine the external flow field around a 3U CubeSat and the internal flowfield of custom pressure sensor ports. The Nonequilibrium Radiative Transport and Spectra Program (NEQAIR) code is used to determine ultraviolet radiation from nitric oxide and the tangent slab approximation is used to estimate spacecraft visible glow radiance from nitrogen dioxide. Additional calculations are performed to provide a sensitivity analysis of radiance estimates based on the DSMC code utilized, chemical reaction rates, and CubeSat orientation.

To my mother and father.

Acknowledgments

This project would not have been possible without the support of many people. Many thanks to my advisor, Dr. Deborah Levin, who read my numerous revisions and helped make sense of the confusion. Thanks to Rose who endured this long process with me, always offering support and love.

Table of Contents

List of Tables

List of Figures

List of Symbols

ϵ	=	Aspect ratio of CubeSat orientation
λ	=	Mean free path, [m]
ν	=	photon frequency, [s^{-1}]
ω	=	viscosity-temperature index
σ	=	total surface accommodation coefficient
σ_f	=	reaction cross section, [m^2]
τ	=	mean time between collisions, [s]
A	=	Einstein A coefficient for spontaneous emission, [s^{-1}]
d	=	diameter of gas molecule, [Å]
C	=	Concentration, [m^{-3}]
E_a	=	Activation energy, [J]
E_c	=	Collision energy, [J]
f	=	Surface flux of particles, [m^{-2}]
g	=	multiplicity of level
h	=	Planck's constant, [$m^2 kgs^{-1}$]
I	=	Radiation intensity, Rayleigh
K	=	transition rate coefficient by collision, [$cm^3 s^{-1}$]
k_B	=	Boltzmann's constant, [JK^{-1}]
K_n	=	Knudsen number
l	=	CubeSat side length, [m]
m	=	number of electronic levels
Ma	=	Mach number
N_ρ	=	number density of particles, [m^{-3}]
P	=	Probability
Q	=	Partition function

$\mathcal{R}$ = Universal gas constant, 8.314 [J mol$^{-1}K^{-1}$]

T = Temperature [K]

u = mass of gas molecule [kg]

x, y, z = Domain coordinates, [m]

Superscripts

A = atomic species collider

M = molecular species collider

r = reverse

Subscripts

iw = heavy-body collision

eq = at equilibrium

h = same species collision partner

ref = reference

s = adsorbed to surface

t = translational

v = vibrational

j = rotational

e = electronic

Chapter 1

Introduction

Designing thermal protection systems (TPS) for spacecraft requires accurate models to describe the thermochemical environment, otherwise considerable margin must be placed on the system to account for uncertainties. While larger design margin increases the likelihood for surviving reentry, the mass and cost of the system escalates and limits resources that could be better used elsewhere in the mission. Testing TPS at flight conditions in ground-based facilities is difficult, so computational models must be used to assess flow conditions [1]. At high altitudes, the continuum flow assumption no longer holds so the statistical Direct Simulation Monte Carlo (DSMC) method developed by Bird [2] is used to model the hypersonic flow and thermal nonequilibrium around a spacecraft during its descent. The high temperatures experienced by the bow shock gas in this flight regime result in chemical reactions, ionization, and radiation that comes from atomic and molecular transitions among electronic excited states. Understanding the mechanisms behind these phenomena and how they change for different flight conditions is essential to improving TPS and reducing the design margin.

The Student Aerothermal Spectrometer Satellite of Illinois and Indiana ($SASSI^2$) will measure the composition of flow in the upper atmosphere by recording the spectral radiation with a suite of visible (VIS) and ultraviolet (UV) spectrometers. Simultaneously, heat flux and pressure on the ram face of the spacecraft will be measured using a sensor package. Over the course of the vehicle's descent through the atmosphere, the spectrometers will take measurements of spectral intensity in the bow shock formed by the spacecraft. The pressure of the gas will be measured using three pressure sensors nested in optimized ports, and the heat flux will be measured from a heat flux sensor positioned on the ram face of the CubeSat. The simulations performed using the DSMC method predict flow characteristics of this experiment such as species number density and temperature, and are used with the Nonequilibrium Radiative Transport and Spectra Program (NEQAIR [3]) to predict the UV and VIS radiation that will be measured by the spectrometers. By obtaining spectral data sets as well as bulk flow properties on a 3U CubeSat, the thermal and chemical environment can be analyzed and used to refine and validate existing computer models.

Previous experiments from sounding rockets and satellites have measured some of the radiation that is

exhibited in these types of flows, but limitations on measurement conditions and instrument effectiveness have yielded an incomplete data set [4, 5, 6]. To the authors' best knowledge, this is the first mission for which spectroscopic data will be gathered onboard a spacecraft reentering the Earth's atmosphere at speeds above 7 km/s since the Fire II mission [4]. Comparison of this data to simulations will improve current and future nonequilibrium models.

Previously, work by Gimelshein et al. [7] and Dogra et al. [8] investigated glow radiation observed about an orbiting spacecraft at altitudes similar to those of the SASSI^2 mission and found that determining the amount of nitric oxide (NO) formed is essential to estimating intensity. While present in small amounts in the ambient atmosphere, the production of NO through an exchange reaction between diatomic nitrogen (N_2) and atomic oxygen (O) is responsible for its concentration in the diffuse shock formed in the ram direction of the satellite. The NO species is also responsible for the formation of nitrogen dioxide (NO_2) on the surface of the spacecraft which is another important contributor to radiation in the visible spectral regime.

In this work, flowfield solutions are shown that study the formation of NO and NO_2 as a function of altitude. A sensitivity analysis is performed to determine dominant chemical reactions in the shock and close to the face of the CubeSat. In a decoupled manner, the radiation in the UV and VIS range are also calculated from the flowfield solution given by DSMC calculations. The sensitivity of flowfield results due to surface accommodation, collisional relaxation, chemical reaction rates, and CubeSat orientation are also shown. Some of the work contained herein was previously presented Ref. [9]. The structure of the thesis is as follows: Chapter 2 illustrates the sensitivity of chemical species to various chemical reaction mechanisms. Chapter 3 presents the numerical methods used for external flow simulations; the initial conditions, domains, and models. Chapter 4 describes the results of the external flow calculations and their sensitivity to changes in modeling parameters, and Chapter 5 contains the results for radiation calculated and the affect of DSMC modeling parameters on simulated spectra. Finally, Chapter 6 contains the conclusions and final remarks.

Chapter 2

Chemical Kinetics

2.1 Batch Reactor Setup

Previous work of Morgan et al. [9] uses a set of five reactions to model the reentry environment, which has been used in earlier modeling work [10]. The set of five reactions used in Ref. [9] did not include mechanisms to reduce the population of NO, which could change the predicted radiation if these processes turned out to be significant. Furthermore, if these reactions were significant, then the previous calculations for nitric oxide (NO) radiation intensity [9] would be overestimated. To determine whether the smaller reaction set chosen for the DSMC simulations was sufficient to predict the concentration of NO, several different calculations are performed using a 0-D chemical heat bath. Reaction rates for different chemical species are used in order to determine their impact on NO formation or dissociation. First, a calculation using the baseline chemical species and rates from the work of Morgan et al. [9] is shown and used to compare and contrast the augmented reaction set. Two different temperatures were chosen as they correspond to different locations in the shock layer in front of the CubeSat. The first temperature, $T_t = 15000K$, is the translational temperature of gas in the shock, further from the ram-face of the CubeSat. The second temperature, $T_t = 8000K$, corresponds to a location close to the stagnation point of the CubeSat where the collision frequency is higher. The heat bath is a unit volume box with fixed temperature, and no inflow or outflow of gas species.

The chemical kinetics are assumed to follow the form of a set of elementary reactions and are listed in Tab. 2.1. Building a system of reactions requires the inclusion of all species and their respective reaction partners, forming a set of differential equations. The concentration at each time level is determined by using the ODE45 solver in MATLAB. The total system of equations is shown below as:

Table 2.1: Chemical Reactions and Rate Expressions.

Reaction	Reference
1. $N_2 + N_2 \xrightarrow{k_{N_2h}} N + N + N_2$	[10]
2. $N_2 + O_2 \xrightarrow{k_{N_2}} N + N + O_2$	[10]
3. $O_2 + O_2 \xrightarrow{k_{O_2h}} O + O + O_2$	[10]
4. $N_2 + O_2 \xrightarrow{k_{O_2}} O + O + N_2$	[10]
5. $N_2 + O \xrightarrow{k_{NO}} NO + N$	[11], [12], [13]
6. $NO + M \xrightarrow{k_d^M} N + O + M$	[11], [14], [15]
7. $NO + A \xrightarrow{k_d^A} N + O + A$	[11], [14]
8. $NO + N \xrightarrow{k_{NO}^r} N_2 + O$	[16]

M is a molecule, A is an atom.

$$\frac{d[N_2]}{dt} = -k_{N_2}[N_2][O_2] - k_{N_2h}[N_2]^2 \tag{2.1}$$

$$\frac{d[O_2]}{dt} = -k_{O_2}[N_2][O_2] - k_{O_2h}[O_2]^2 \tag{2.2}$$

$$\frac{d[O]}{dt} = 2k_{O_2}[N_2][O_2] + 2k_{O_2h}[O_2]^2 - k_{NO}[N_2][O] + k_{NO}^r[NO][N] \tag{2.3}$$

$$\frac{d[N]}{dt} = 2k_{N_2}[N_2][O_2] + 2k_{N_2h}[N_2]^2 + k_{NO}[N_2][O] + k_d^M[NO][M] + k_d^A[NO][A] \tag{2.4}$$

$$\frac{d[NO]}{dt} = k_{NO}[N_2][O] - k_d^M[NO][M] - k_d^A[NO][A] - k_{NO}^r[NO][N] \tag{2.5}$$

where the forward reaction rates, k, correspond to the rates Reactions 1 - 7. The reverse reaction rate, k^r, is the reverse Zel'dovich process that is modeled with the rates of Dikalyuk [16].

Three cases are studied to determine the effect different processes have on the concentration of NO. Case 1 is the baseline set of reactions used in Ref. [9] that only models NO production through Reaction 5. Case 2 adds to Case 1 by including Reactions 6 and 7 which are mechanisms for NO dissociation. Case 3 includes the processes of Case 1 and Case 2 as well as Reaction 8, which is the reverse Zel'dovich process. For all cases, Reactions 1 - 4 are used. The case numbers and their description are summarized in Tab. 2.2.

Table 2.2: Case Description.

Case	NO Reaction Used (#)
1	5
2	5,6,7
3	5,6,7,8

2.2 Case 1

For this set of reactions used, only Reactions 1 - 5 are modeled. The only process that affects the concentration of NO is Reaction 5. This set of reactions is the most optimistic estimation of NO formation and represents an upper-bound to what is expected of NO formation, which was previously modeled in Ref. [9]. Figure 2.1 shows the time evolution of all five species concentrations where the concentration of NO and N increase due to the Zel'dovich process. Also shown in the figure is the gradual reduction of the diatomic species concentrations (O_2, N_2) which is because only the dissociation reaction for the molecular species is used. Shown in Fig. 2.2(a) and Fig. 2.2(b) are the relative times to reach equilibrium using three different reaction rates for the Zel'dovich reaction. As seen previously in Ref. [9], the rate of Park is greater for higher temperatures which leads to the NO concentration reaching steady state earlier.

At lower temperatures where most of the gas phase collisions occur, the rate of Baulch is greater. A newly considered reaction rate that is derived from quasi-classical trajectory (QCT) rates similar to the rates developed by Bose and Candler [17] is also shown from the work of Luo et al [13]. The rates calculated by Luo et al. are similar to the rates of Park and Baulch at lower temperatures, but predict higher rates of NO formation for both temperatures simulated, $T_t = 10000K$ and $T_t = 8000K$, which can be seen clearly from Fig. 14(a) in Ref [13]. Despite the change in rates, the final concentration of the species is still the same because the equilibrium state is determined by the processes considered.

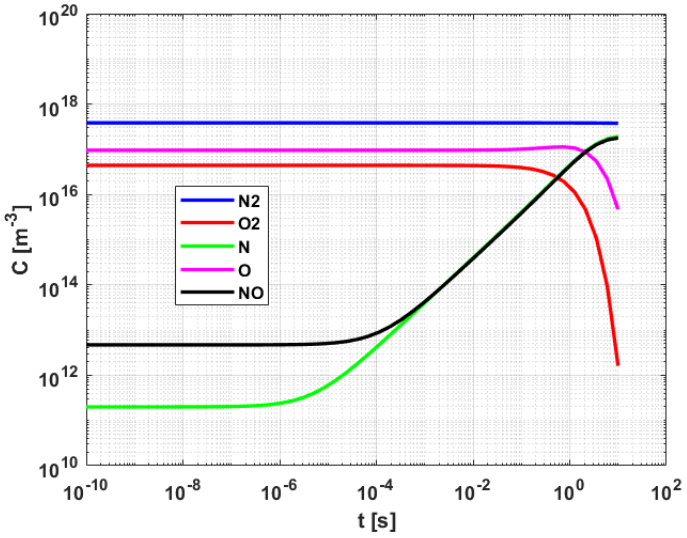

Figure 2.1: Time evolution of 5-species concentrations at $T_t = 8000K$, total $N_\rho = 5.22 \times 10^{17}$ m^{-3}.

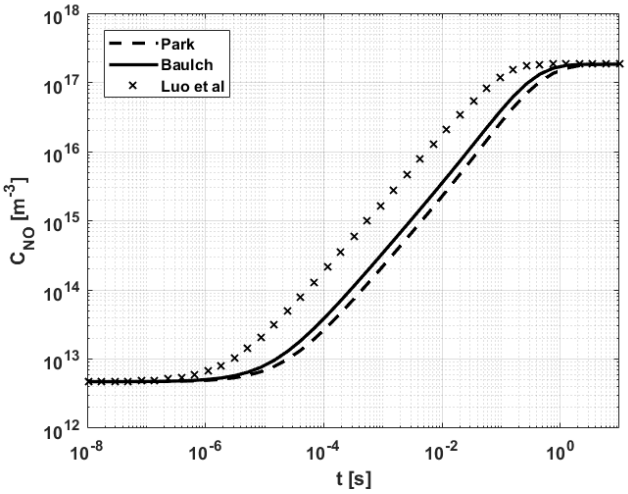

(a) Nitric oxide concentration time evolution at $T_t = 15000K$.

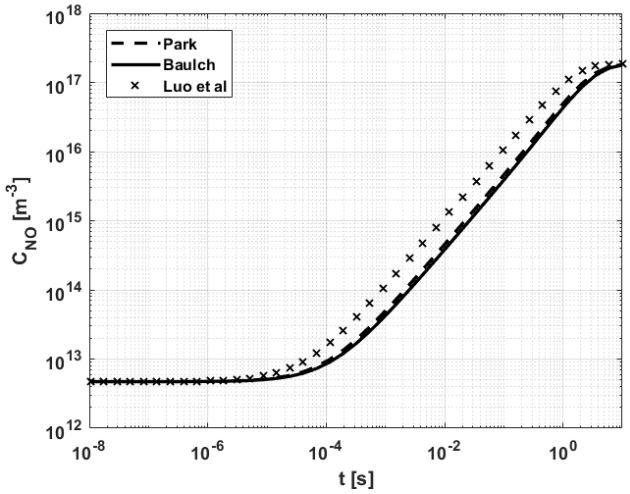

(b) Nitric oxide concentration evolution at $T_t = 8000K$.

Figure 2.2: Comparison of NO formation rates at two different temperatures.

2.3 Case 2

The second simulation includes Reactions 6 and 7, the reactions by which NO is dissociated by colliding with other gas species. For this simulation, Reaction 5 uses the rates of Baulch [12]. The legacy set of Park [11] and new reaction set of Cruden [14] were chosen to study the dissociation of NO due to molecular and atomic colliders. For these rates, the geometric average temperature is used, as suggested by Park [11], where:

$$T_{ave} = \sqrt{T_t T_v} \tag{2.6}$$

where T_t and T_v is the translational and vibrational temperatures of the gas molecules, respectively.

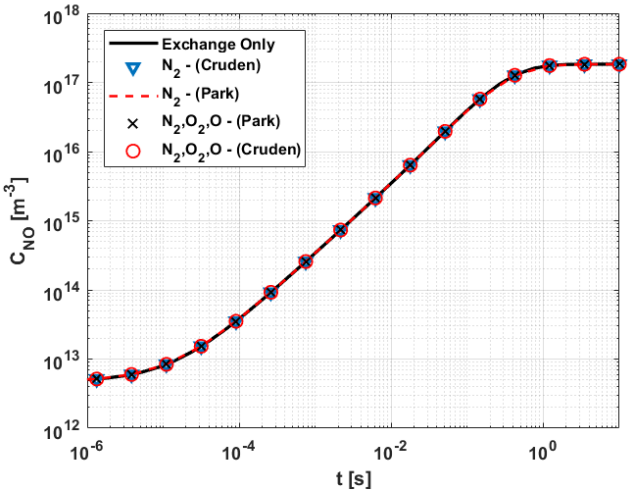

(a) Nitric oxide concentration time evolution at $T_t = 15000K$.

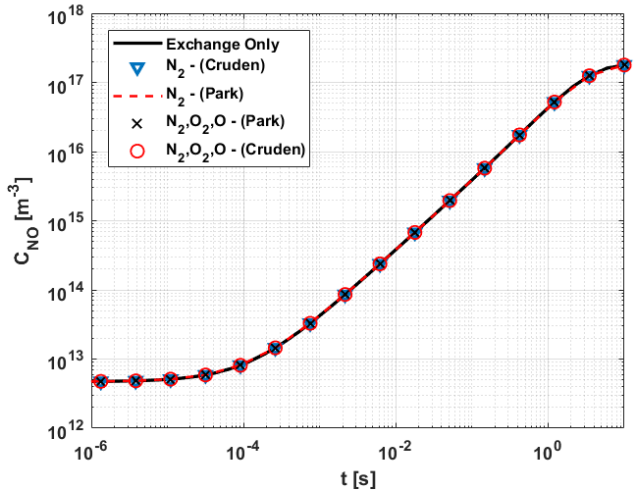

(b) Comparison of Baulch and Park rates at $T_t = 8000K$.

Figure 2.3: Comparison of NO concentration at two different temperatures, for Reactions 1 - 7.

Initially, only the collisions between N_2 and NO are considered, as N_2 is the most common species in the flow. The expression for Reactions 6 and 7 that follow are shown as:

$$k_d^M[\mathrm{NO}][\mathrm{M}] = k_d^M[\mathrm{NO}][\mathrm{N_2}] \tag{2.7}$$

$$k_d^A[\mathrm{NO}][\mathrm{A}] = 0 \tag{2.8}$$

Shown in Figs. 2.3(a) and 2.3(b), using the rate of Cruden (blue triangles) or the rate of Park (dashed red) for NO dissociation has negligible impact on the concentration of NO for all time. This is due to the

use of the average temperature T_{ave}, which is lower than the translational temperature since the internal temperature for the gases is relatively cold, as shown in Ref. [8, 9]. Since the rate parameters for Reactions 6 and 7 do not depend on the species used, a total rate of dissociation due to molecular and atomic collisions can be calculated by including the concentration of other species:

$$k_d^M[\mathrm{NO}][\mathrm{M}] = k_d^M[\mathrm{NO}][\mathrm{N_2}] + k_d^M[\mathrm{NO}][\mathrm{O_2}] \tag{2.9}$$

$$k_d^A[\mathrm{NO}][\mathrm{A}] = k_d^A[\mathrm{NO}][\mathrm{O}] \tag{2.10}$$

Using the above calculated rate for NO dissociation leads to a factor of 6 difference in the total dissociation rate, but Figs. 2.3(a) and 2.3(b) show (black crosses, red circle) that this larger rate still does not have a strong impact on the rate of change in the NO concentration or the final equilibrium concentration.

2.4 Case 3

The final simulation includes all processes, Reactions 1 - 8. For Reaction 5, the rate of Baulch [12] are still is used. The dissociation reactions, Reaction 6 and 7, are modeled using the rates of Park [11] considering the molecular species to be N_2, and the atomic species to be O. Reaction 8, the reverse Zel'dovich process, is modeled using the rate of Dikalyuk [16].

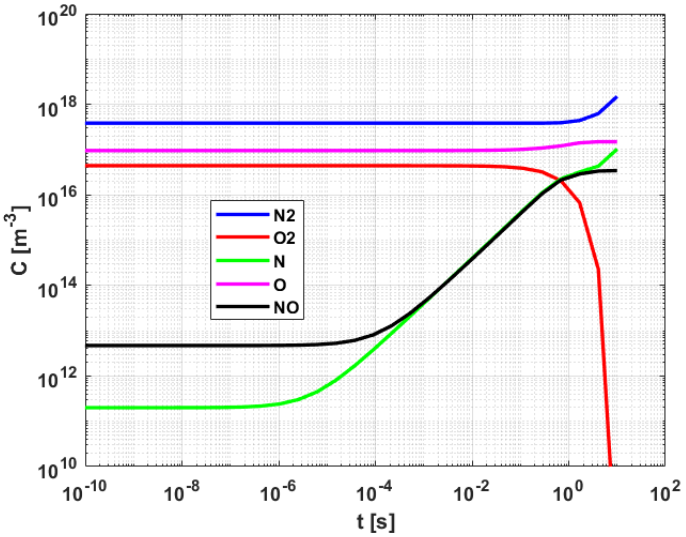

Figure 2.4: Time evolution of 5-species concentrations at $T_t = 8000K$, total $\mathrm{N}_\rho = 5.22 \times 10^{17}$ m^{-3}.

Figure 2.4 shows the time evolution for all five species in the heat bath simulation. In this simulation, concentrations of NO and N are reduced by collisions with N_2 and O, as well as through the reverse Zel'dovich

process. At $t \approx 1s$, the concentrations of O and N_2 begin to increase as more NO is destroyed by Reactions 6 - 8 than created by Reaction 5. The population of N still increases because the largest contributor to the rate of change is Reaction 1, though the rate at which the concentration changes decreases for a short time after $t \approx 1s$. Still, there is no mechanism for O_2 to be produced so the concentration tends to zero as the simulation continues.

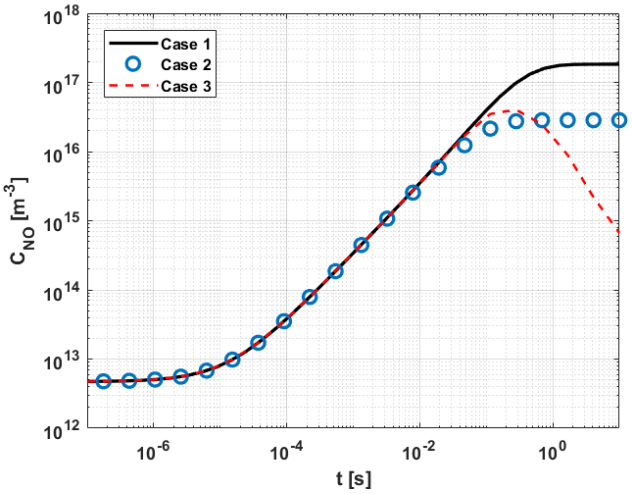

(a) Nitric oxide concentration time evolution at $T_t = 15000K$.

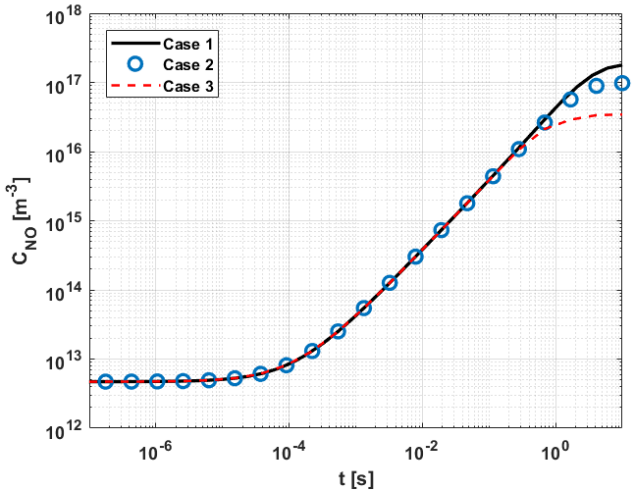

(b) Nitric oxide concentration evolution at $T_t = 8000K$.

Figure 2.5: Comparison of Case 1, 2, and 3 for two different temperatures.

To compare with previous simulations, Figs. 2.5(b) and 2.5(a) show the time evolution of the NO concentration for Case 1, 2, and 3. For Case 1 and 2, Reaction 5 uses the rates of Baulch [12]. For Case 2, the dissociation mechanism is modeled using only Reaction 6 now with the rate of Andrienko [15]. The dissociation rate is found by using a simplified QCT model that does not depend on the average temperature,

but rather the translational temperature, T_t. As a result, the rate of Andrienko [15] is higher than both the rates of Cruden [14] and Park [11]. Still, the total rate of change of NO due to dissociation depends on the concentration of NO, which remains relatively low for most of the time simulated. From Fig. 2.5(a) and Fig. 2.5(b), the effect of increasing the temperature is once again illustrated by the time elapsed before differences in NO concentration are observed. The peak NO concentration for each case occur now at $t = 0.1s$ at $T_t = 15000K$ compared to $t = 1s$ at $T_t = 8000k$.

For all of the reactions modeled, notable differences in species concentration occur after at least 100 ms have elapsed. For the conditions simulated, the equilibrium time between collisions is:

$$\tau = \frac{1}{4d_{ref}^2 N_\rho \left(\frac{\pi k T}{u}^{0.5}\right)\left(\frac{T_{ref}}{T}^{1-\omega}\right)} \tag{2.11}$$

where d_{ref} is the reference diameter for a molecule of gas. N_ρ is the number density of the gas, and ω is the viscosity-temperature index of the gas. For the total number density considered, the minimum time between collisions occurs with the lowest temperature, $T_t = 8000k$, and has a value of $\tau = 1.5 \times 10^{-2}$ s. Not all collisions have enough energy to dissociate NO or undergo an exchange reaction so there may be many collisions before the NO molecule is destroyed. In the context of a CubeSat during reentry, by the time such an event occurs, new gas particles have entered the bow-shock interaction zone and formed NO. Because of this, the change in NO concentration past $t = 0.1s$ where the slow reverse Zel'dovich reaction begins to affect the NO concentration is not relevant to the short times at which particles reside in the shock interaction zone.

Chapter 3

DSMC Numerical Methods

3.1 External Simulation Setup

The simulations of the CubeSat are performed using the DSMC Stochastic PArallel Rarefied-gas Time-accurate Analyzer (SPARTA [18]) and Statistical Modeling in Low-Density Environment (SMILE [19]) codes. Calculations are performed for external flow over the CubeSat for altitudes from 100 to 200 km because this is the transitional regime of flow where measurements will be recorded by the UV and VIS spectrometers. Measurements by the VIS spectrometer will take place starting at an altitude of 200km and will continue to 150 km. Below 150km, ultraviolet radiation will be recorded by two UV spectrometers. Based on trajectory analyses, the velocity of the CubeSat for these altitudes will be approximately 7.55 km/s. The freestream conditions used for the simulations are given in Tab. 3.1 and the list of reactions that are considered for the external flow simulations are listed in Tab. 3.2 from Refs. [7] and [10]. The initial freestream mole fractions at each altitude are shown in Tab. 3.3. For these simulations, the mole fractions for the major species are from Jacchia [20] and the trace species are from the results of McCoy [21].

Table 3.1: Flow Simulation Parameters[a].

Freestream Parameter	External Simulations								
Altitude (km)	200	180	160	150	140	130	120	110	100
Freestream Temperature (K)	1026	947	822	730.6	625	500	368	247	195
λ(m)	250	170	66	40	22	10	3.4	0.77	0.13
Knudsen Number[b]	5000	3400	1320	800	442	201	69.6	15.5	2.6
Mach	10.2	10.8	11.8	12.7	13.9	15.7	18.6	23.1	26.5

[a] A surface temperature of 300 K and a spacecraft velocity of 7,550 m/s were assumed.
[b] Knudsen number for external flow simulations calculated using the edge length of the ram-face of the simulated CubeSat.

The passive stability of the CubeSat will keep the ram face within an angle-of-attack of $\pm$ 2 degrees [23]. Since the flow is then symmetric across two planes, only a quarter of the domain needs to be simulated. The simulated geometry of the 3U CubeSat is shown in Fig. 3.1(a). The baseline orientation of the CubeSat is shown in Fig. 3.1(b) where the ram face is located at the origin; Fig. 3.1(c) shows the broadside orientation.

Table 3.2: Chemical Reactions used for External DSMC Calculations[c].

Reaction	a, m^3/s	n	E_a(J)
$O_2 + N_2 \rightarrow O + O + N_2$	3.320×10^{-9}	-1.5	8.214×10^{-19}
$O_2 + O_2 \rightarrow O + O + O_2$	3.320×10^{-9}	-1.5	8.214×10^{-19}
$O_2 + N_2 \rightarrow N + N + O_2$	4.981×10^{-8}	-1.6	1.563×10^{-18}
$N_2 + N_2 \rightarrow N + N + N_2$	1.162×10^{-8}	-1.6	1.563×10^{-18}
$N_2 + O \rightarrow NO + N$	1.070×10^{-12}	-1.0	5.175×10^{-19}
[b]$N_2 + O \rightarrow NO + N$	1.12×10^{-16}	0.0	5.175×10^{-19}
$O_2 + N \rightarrow NO + N$	4.134×10^{-12}	1.180	5.530×10^{-20}

[a]Reaction rates assume the form, $k_f = aT^n \exp(-E_a/k_B T)$.
[b]Rate is from Ref. [12].
[c]Rates are from Ref. [10].

Table 3.3: Atmospheric Composition used for External[a] and Internal[b] CubeSat Flow Simulations.

Altitude (km)	N_ρ (m^{-3})	N_2	O_2	N	O	NO
100	1.20×10^{19}	0.776	0.1746	3×10^{-8}	3.84×10^{-2}	3×10^{-6}
110	2.13×10^{18}	0.767	0.1227	1.8×10^{-7}	0.11	9×10^{-6}
120	5.24×10^{17}	0.73	8.43×10^{-2}	3.82×10^{-7}	0.182	3.44×10^{-5}
130	1.58×10^{17}	0.64	7.13×10^{-2}	5.28×10^{-6}	0.286	2.20×10^{-10}
140	9.34×10^{16}	0.65	6.18×10^{-2}	5×10^{-5}	0.29	8×10^{-5}
150	5.31×10^{16}	0.62	5.46×10^{-2}	2×10^{-4}	0.33	9×10^{-5}
160	3.35×10^{16}	0.58	4.86×10^{-2}	1×10^{-3}	0.37	11×10^{-5}
180	1.62×10^{16}	0.49	3.89×10^{-2}	3×10^{-3}	0.47	15×10^{-5}
200	9.06×10^{15}	0.45	3.13×10^{-2}	6.62×10^{-3}	0.51	11×10^{-5}

[a]Refs. [20, 21].
[a]Ref. [22]

Depending on the altitude simulated, the size of the domain was changed to capture the bow shock region. Figure 3.2 shows the temperature profile at different altitudes. In order to successfully capture features of the rarefied flow, the domain size, cell size, and timestep are varied. The 100 km case had the smallest domain size at $(0.4 \times 0.2 \times 0.2)$m because of the thickness of the shock simulated. The maximum domain size of at $(2.4 \times 1.0 \times 1.0)$m is used for the simulations at and above an altitude 140 km case because the shock thickness does not change at higher altitudes enough to warrant a larger domain. Simulations are allowed to run until macro parameters reach steady state and then sampling occurs at each timestep once steady state is achieved.

3.1.1 Chemical Reactions

Gas-Phase Reactions

In both the SMILE and SPARTA codes, chemical reactions are modeled using the total collision energy (TCE) model of Bird [2]. The TCE model accepts reaction rates in a modified Arrhenius form in order

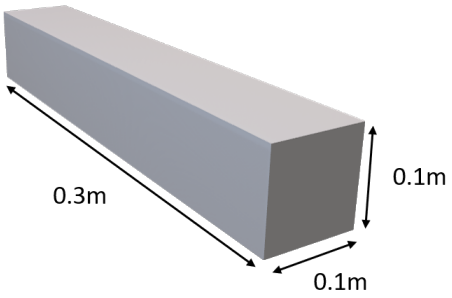

(a) Simulated 3U CubeSat geometry.

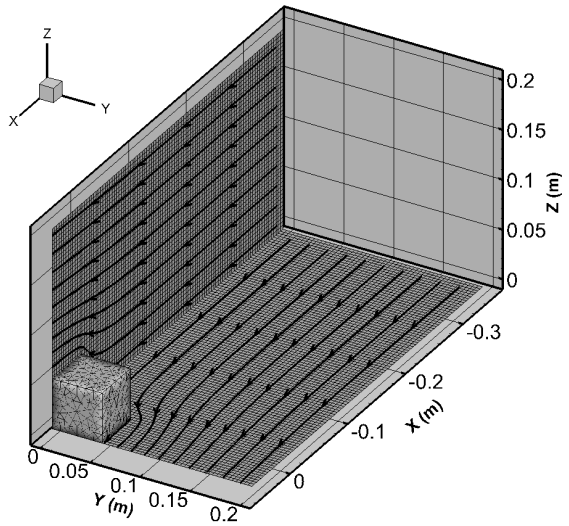

(b) Baseline orientation of the CubeSat, $\epsilon = 0.33$.

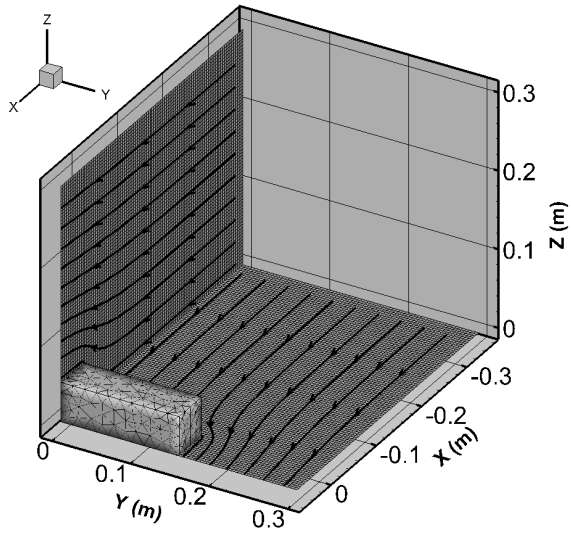

(c) Broadside orientation of the CubeSat, $\epsilon = 3$.

Figure 3.1: Simulated CubeSat in quarter-domain at 100km with flow in the +X direction.

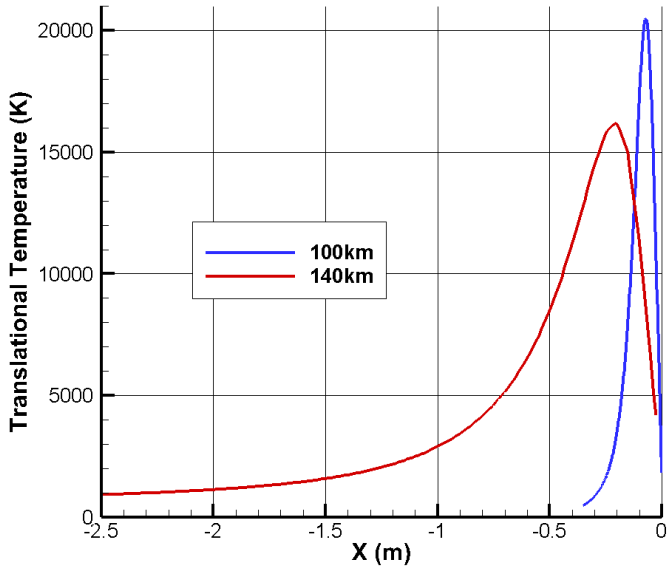

Figure 3.2: Translational temperature profiles for 100 km and 140 km using SPARTA, for $\epsilon = 0.33$, and using the rates of Park.

to use experimental reaction rates. In the TCE model, a colliding pair has a finite probability for reaction when the relative collision energy exceeds the activation energy. For the conditions simulated, the dominant mechanism for producing NO is through the Zel'dovich reaction:

$$N_2 + O \xrightarrow{k_f} NO + N \tag{3.1}$$

This reaction, versus other possible exchange reactions to produce NO, is the dominant reaction because of the free stream mole fraction of species present. For the conditions simulated, N_2 and O are major species and neither the reaction for dissociation of N_2 or O_2 are strong enough to cause other exchange reactions to be significant.

Gas-Surface Reactions

The surface of the CubeSat is made of a metal oxide. The incident O and NO molecules on the surface results in these species being adsorbed on the surface on the available surface sites. The surface reactions

used in this work for O and NO species are summarized as follows [7, 8]:

$$\mathrm{NO} + S \longleftrightarrow \mathrm{NO_S} \tag{3.2}$$

$$\mathrm{O} + S \longleftrightarrow \mathrm{O_S} \tag{3.3}$$

$$\mathrm{NO_S} + \mathrm{O} \xrightarrow{k_{f_{3.4}}} \mathrm{NO_2^*} + S \tag{3.4}$$

$$\mathrm{NO} + \mathrm{O_S} \xrightarrow{k_{f_{3.5}}} \mathrm{NO_2^*} + S \tag{3.5}$$

$$\mathrm{NO_S} + \mathrm{O_S} \xrightarrow{k_{f_{3.6}}} \mathrm{NO_2^*} + S, \tag{3.6}$$

where S represents a surface site on the metal oxide surface. The adsorption-desorption reactions numbered 3.2 and 3.3 are reversible. Reactions 3.4 and 3.5 follow an Eley-Rideal mechanism where one of the species is in the gas phase and the other is adsorbed on the surface. Reaction 3.6 follows a Langmuir-Hinshelwood mechanism where all the reactants are adsorbed on the surface and can diffuse between surface sites to form products [24].

The forward (adsorption) rate for Reactions 3.2 and 3.3 is determined from the sticking probability of NO and O species on the surface. Their backward (desorption) rate is, however, determined based on their heat of desorption [7]. Since the heat of adsorption for O is about five times smaller than that of NO, O atoms have a very low residence time on the surface making Reaction 3.4 the most dominant for producing $\mathrm{NO_2^*}$. A value of 16 kcal/mol for the heat of adsorption of O in the surface is used in this work. At steady state, surface coverage of NO reaches a constant value with a constant O and NO flux incident on the surface. Since the reaction rates for gas-surface reactions are much smaller compared to that of gas-phase reactions, the gas-surface processes are assumed to be decoupled from the gas-phase calculations and use O and NO surface fluxes obtained from the DSMC gas phase calculations.

3.1.2 Radiation Calculations

Visible Radiation

The primary source of visible radiation around the CubeSat is considered to be $\mathrm{NO_2^*}$ [7, 25]. Molecules of $\mathrm{NO_2^*}$ are formed on the surface of the CubeSat as per the surface chemical reactions 3.2-3.6. The tangent slab approximation model is used for estimating visible radiation due to $\mathrm{NO_2^*}$. This model is used in Ref. [7] where radiation intensity is given by,

$$I = \frac{\sigma_{f_{3.4}} n_{\mathrm{NO_x}} f_{\mathrm{O}} + \sigma_{f_{3.5}} n_{\mathrm{O_x}} f_{\mathrm{NO}}}{2}, \tag{3.7}$$

where f_{O} and f_{NO} are the fluxes of O and NO on the surface, $n_{\mathrm{NO_x}}$ and $n_{\mathrm{O_x}}$ are the surface number density (molecules/m^2) of NO and O adsorbed on the surface, and σ_{f4} and σ_{f5} are the cross sections of surface reactions 3.4 and 3.5. The spacecraft glow calculations are performed using the steady state DSMC solutions for the CubeSat geometry. The radiance due to NO_2^* produced on the surface will be discussed in Section 5.

UV Radiation

The primary source of ultraviolet radiation is expected to be from NO (γ)-band radiation [21, 26]. NO(γ)-band radiation is produced by the $A^2\Sigma^+ \rightarrow X^2\prod$ transition, so in order to estimate the radiative intensity, the population density of NO(A) state must be determined. At these altitudes, there are insufficient collision to form a Boltzmann distribution and therefore the mechanisms for populating the excited electronic states must be specified. In this work, only heavy-body collisional processes are considered as the degree of ionization is assumed to be very low. Future work will study this assumption by including excitation and deexcitation processes due to electron impact. The specific processes by which NO may be excited and deexcited are given as:

$$\mathrm{NO}(i) + \mathrm{W} \xrightarrow{K(i,j)} \mathrm{NO}(j) + \mathrm{W} \tag{3.8}$$

$$\mathrm{N} + \mathrm{O} + \mathrm{W} \xrightarrow{K_{\mathrm{Wi}}} \mathrm{NO}(i) + \mathrm{W} \tag{3.9}$$

$$\mathrm{NO}(i) \xrightarrow{A(i,j)} \mathrm{NO}(j) + h\nu \tag{3.10}$$

where $K(i,j)$ for Reaction 3.8 is the neutral impact excitation rate coefficient for $i < j$ and deexcitation rate coefficient if $i > j$. In Reaction 3.9, K_{wi} is the heavy-body recombination rate coefficient while K_{iw} is the rate coefficient due to heavy body dissociation caused by species W, where W is another heavy particle. The last process considered for excitation and deexcitation is Reaction 3.10, where $A(i,j)$ is the spontaneous emission rate coefficient from electronic level i to j. To determine the number of NO molecules in each excited state, the reactions form a system of master equations given by Park[1] as:

$$\begin{aligned}\frac{\partial N_i}{\partial t} = &\sum_{j=1}^{m} K(j,i)N_j N_W + \sum_{j=1}^{m} A(j,i)N_j + K_{Wi}N_O N_N N_W \\ &- \sum_{j=1}^{m} K(i,j)N_i N_W - \sum_{j=1}^{m} A(i,j)N_i - K_{iW}N_W N_i\end{aligned} \tag{3.11}$$

When the rate of change of N_i is very small, the condition is known as the quasi-steady-state (QSS) condition, and the left hand side is equated to zero. The simplification of Eq. 3.11 allows for the excitation and deexcitation quantities to be put into matrix form so that the system of equations can be solved for the

vector N, the number density of the ith electronic level:

$$M\bar{N} = C \tag{3.12}$$

The diagonal elements of M are:

$$M(i,i) = \sum_{j=1}^{m} \left(K(i,j) + \frac{A(i,j)}{N_W} \right) + K_{iW} \tag{3.13}$$

and the off-diagonal elements of M are:

$$M(i,j) = -K(j,i) - \frac{A(j,i)}{N_W} \tag{3.14}$$

The elements of vector C are:

$$C(i) = K_{Wi} N_N N_O \tag{3.15}$$

As a simplification, the conservation equation, Eq. 3.16 may be substituted in for the $i = 1$ level of the QSS equation:

$$\sum_{j=1}^{m} N_i = N_{NO} \tag{3.16}$$

which corresponds to matrix values of $M(1,j) = 1$ and $C(1) = N_{NO}$. The vector $\bar{N}$ is determined by inverting the $m \times m$ matrix M and multiplying with the column vector C.

Chapter 4

Direct Simulation Monte Carlo Results

4.1 External Flowfield Sensitivity Analysis

To quantify the variance of predicted NO formation as the CubeSat descends through Earth's atmosphere, external simulations are performed with several different parameters. Table 4.1 summarizes the DSMC numerical parameters considered for the different altitudes and cases considered, and the figures shown are at an altitude of 120km. The order of the sensitivity analysis is chosen in ascending order of its effect on the mole fraction of NO.

Table 4.1: Case Definitions for Sensitivity Analysis of External Simulations[a].

Case (#)	DSMC Code	ϵ	Zel'dovich Rate	σ
$1(a)$	SPARTA	0.33	Park	1.0
$1(b)$	SPARTA	0.33	Park	0.9
$2(a)$	SPARTA	0.33	Baulch	1.0
$2(b)$	SMILE	0.33	Baulch	1.0
3	SPARTA	3.0	Baulch	1.0

[a]Cases shown are for an altitude of 120 km.

4.2 Surface Accommodation Coefficient

Figure 4.1(a) shows the translational and internal temperatures predicted for both altitudes along the stagnation line in the shock region using SPARTA. The ram face of the CubeSat is located at the origin as seen in Figs. 3.1(b) and 3.1(c). For high altitudes where N_2 is the dominant species, the rarefaction results in a large mean time between collisions which results in a low chance for particles to exchange energy with internal modes, which is similar to the result observed by Dogra et al [8]. The vibrational and rotational temperature do not significantly change for $\sigma = 0.9$ when compared to $\sigma = 1.0$. The translational temperature varies significantly for different values of σ because of the difference in velocities for reflected particles. When $\sigma = 1.0$, particles are emitted from the surface with a most probable speed equal to the surface temperature of 300 K. When $\sigma = 0.9$, 10% of incident particles retain their energy after striking the surface. The small

fraction of these highly energetic reflected particles then changes the average kinetic energy of the particles in each cell. Since the flow is highly directional for both altitudes, the translational temperature is elevated significantly along the stagnation line. Since the internal temperatures do not change significantly when changing other simulation parameters, they are not shown in the remaining figures. Presented in Fig. 4.1(b) is the number density profile along the stagnation line for Cases 1(a) and 1(b) and it can be seen the that the mole fraction does not change significantly along the stagnation line. The sensitivity of radiation produced in the UV and VIS regime to thermal accommodation coefficient will be investigated in future work.

4.3 Chemical Reaction Rates

Two different reaction rates are used to assess NO production sensitivity to different rates for the Zel'dovich reaction. The rates used come from the set of Park [10] and Baulch[12], and were used in the earlier works [8, 10]. The reaction rates have the same activation energies as can be seen in Tab. 3.2, but have a somewhat different temperature dependencies as seen in Fig 4.2. At higher temperatures the forward reaction rate coefficient, k_f, is higher for the rates of Baulch [12] than the rates of Park [10]. Even though the temperature remains nearly the same as seen in Fig. 4.3(a), Fig. 4.3(b) shows the change in NO mole fraction due to variation of the chemical reaction rate. When the rate given by Park [10] is used, more NO is produced in the shock region than when using the rates of Baulch [12]. The mole fraction of NO increases in the region close to the body (near the origin) when using the rates of Park [10] because the rate is higher for the gas temperature close to the body where most collisions occur. The concentration of the free stream NO is nearly recovered upstream of the shock, where particles can no longer diffuse and the reactions are not as likely.

4.4 CubeSat Orientation

To investigate the flowfield dependence on CubeSat orientation, simulations are performed with the CubeSat oriented 90 degrees to its current flow orientation using both SMILE and SPARTA. Figure 3.1 shows the two different CubeSat orientations used in this analysis, and the corresponding aspect ratio:

$$\epsilon = \frac{l_{normal}}{l_{edge}} \tag{4.1}$$

where l_{normal} and l_{edge} are the longest edge length of the face normal and parallel to the flow respectively. It can be seen from Fig. 4.4 that by altering the orientation of the CubeSat, the size of the diffuse shock

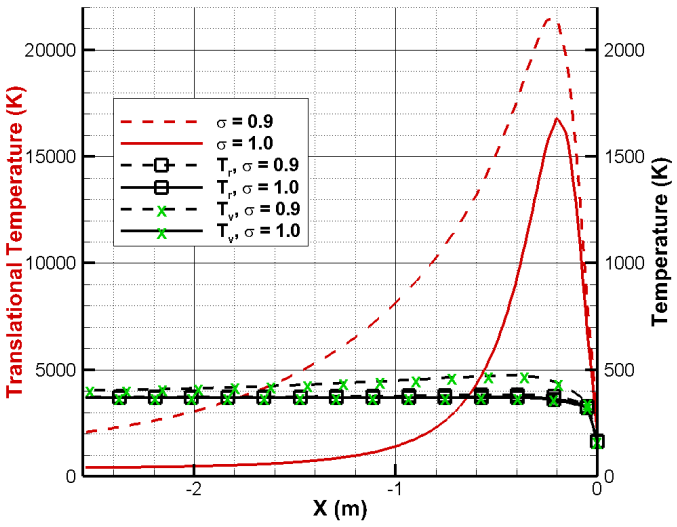

(a) Temperature profiles in the shock region for different values of σ.

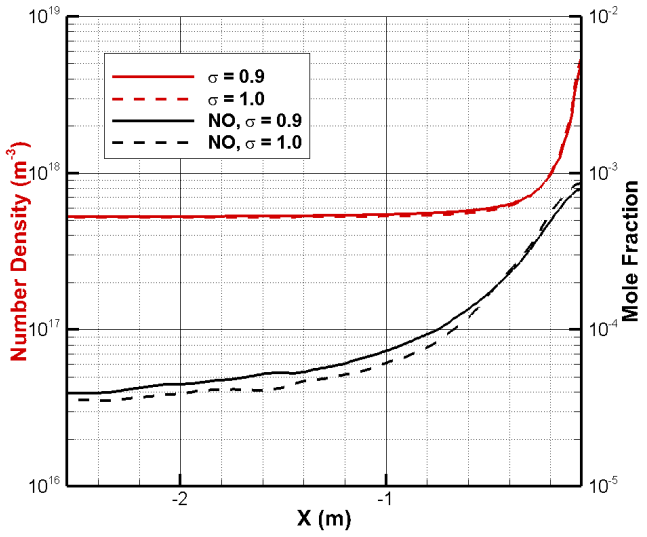

(b) Stagnation line total number density and mole fraction of NO for two different values of σ.

Figure 4.1: Comparison of stagnation streamline macro parameters for Cases 1(a) and 1(b).

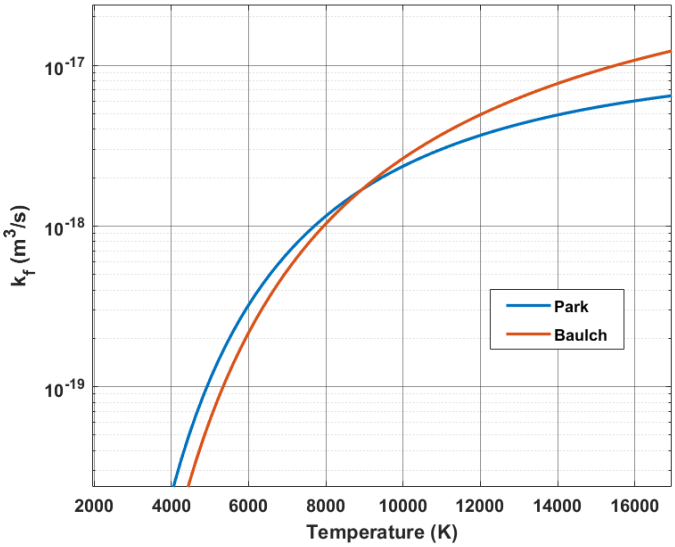

Figure 4.2: Forward rate coefficient change with temperature for the Zel'dovich reaction from the set of Park and Baulch.

interaction region changes. The increase in NO production is due to the larger area that freestream particles can strike. Increasing the number of particles that strike the surface, increases the number of reflections. The subsequent increase in gas-gas collisions broadens the shock as shown in Fig. 4.4(a), and the increase in number of collisions promotes the formation of NO which can be seen in Fig. 4.4(b).

4.5 Model Differences

Although both the SMILE and SPARTA codes use the TCE model, their implementations differ. For one, in the SPARTA code, the TCE model uses an effective internal degree of freedom equal to one as demonstrated by Bird [2]. Figure 4.5 shows the difference in probability for the Zel'dovich reaction to occur after being considered for reaction and it can be seen that for each colliding pair with sufficient collision energy, the expression used by the SPARTA code results in a higher probability for the reaction to take place. Additionally, in the post-collision relaxation calculation, SPARTA uses a constant vibrational degree of freedom equal to two, whereas the SMILE code uses a temperature dependent vibrational degree of freedom.

The model differences result in slightly different shock thicknesses. SPARTA predicts shocks that are slightly more diffuse as shown in Fig. 4.6(a). The large increase in predicted NO number seen in Fig. 4.6(b) arises from the difference in probability for a reaction to occur between the SPARTA and SMILE codes, which comes from the different effective internal degrees of freedom and temperatures employed.

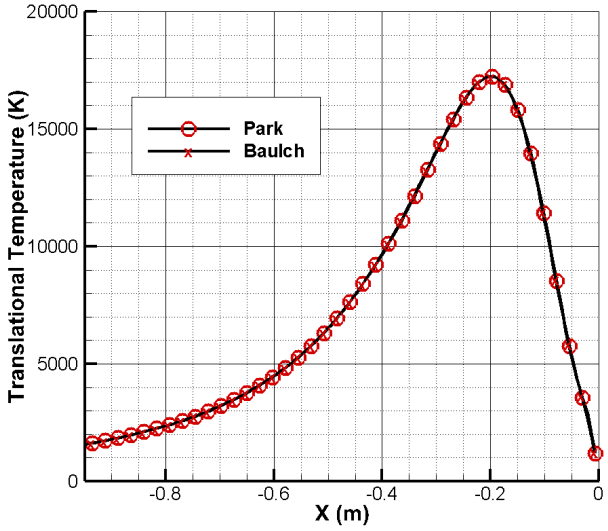

(a) Stagnation line translational temperature profile for two different Zel'dovich reaction rates.

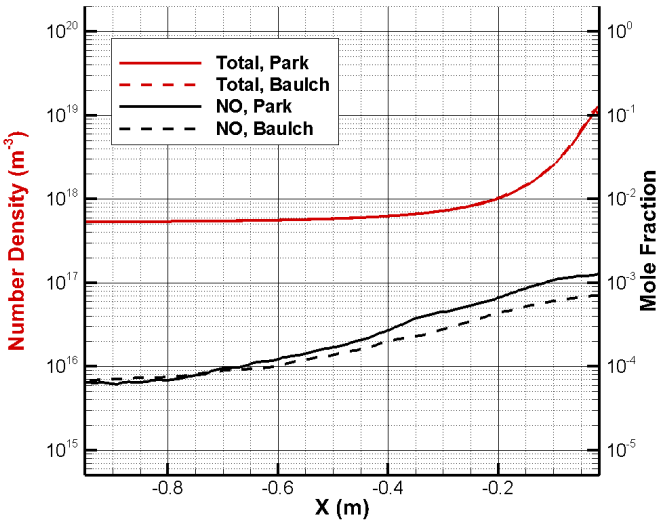

(b) Stagnation line total number density and mole fraction of NO for two different Zel'dovich reaction rates.

Figure 4.3: Comparison of stagnation streamline macro parameters for Cases 1(a) and 2(a).

4.6 Summary

The mole fraction dependence on altitude can be summarized, as shown in Fig. 4.7, and it is apparent that the predicted flowfield is most sensitive to the different models employed in solving for flow over the CubeSat for these altitudes by comparing the curve for SPARTA (dashed green) and SMILE (solid green). The next

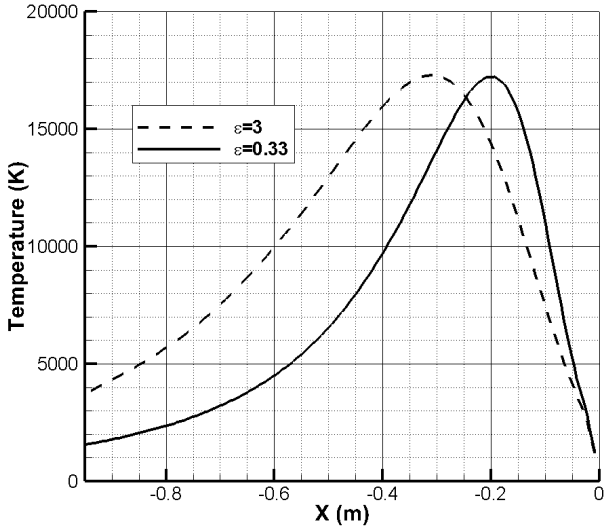

(a) Stagnation line translational temperature profile for two different aspect ratios, ϵ.

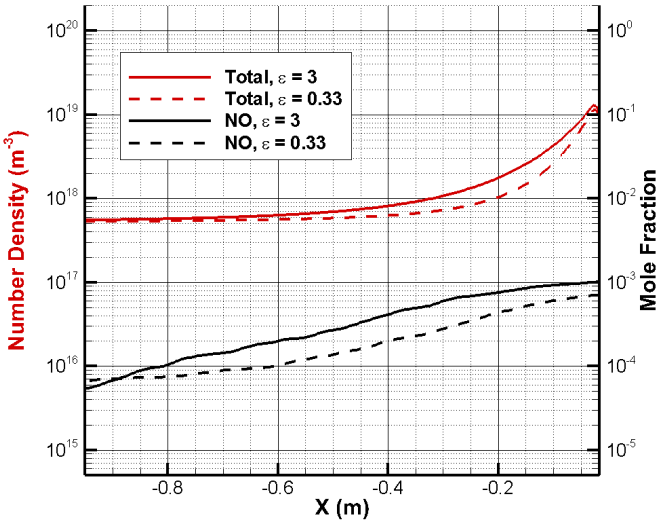

(b) Stagnation line total number density and mole fraction of NO for two different aspect ratios, ϵ.

Figure 4.4: Comparison of stagnation streamline macro parameters for Cases 2(a) and 3.

most significant parameter that effects the production of NO for a given flowfield is the aspect ratio of the geometry (solid magenta and solid green), or the ratio of surface area available for reflections compared to the stream-wise length of the body. Finally, the differences in NO production for two different rates of the Zel'dovich reaction yield are shown (dashed square and dashed delta) and it is seen from here that the

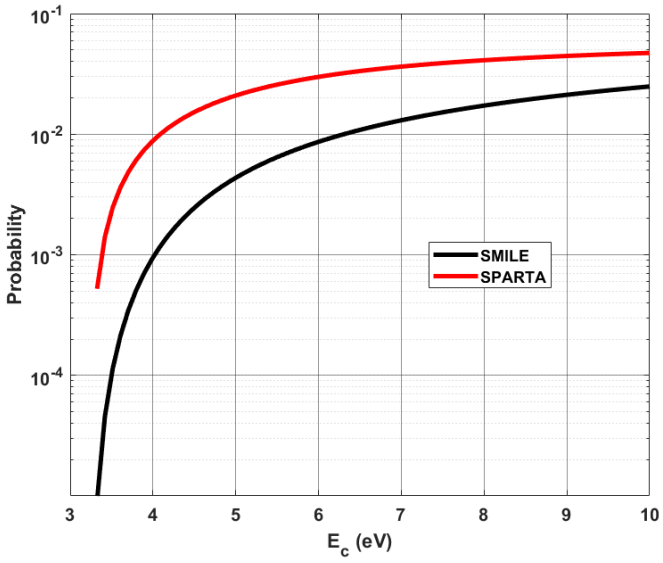

Figure 4.5: Probability for Zel'dovich exchange reaction of Park to take place using SPARTA and SMILE.

differences vary across the range of altitudes. As the CubeSat descends to lower altitudes, the shock region becomes thinner and the peak temperature in the shock is raised when the speed is maintained. For higher temperatures, the reaction rate coefficient of Park [10] will become larger, leading to greater differences in predicted NO mole fractions. The mole fraction of produced NO depends on N_2 and O, the reactants of the first Zel'dovich reaction (Reaction 3.1). Owing to the low reaction-rate of N_2 dissociation, nearly all of N_2 in the domain is available for Reaction 3.1. On the other hand, availability of O in the domain is affected by the mole fraction of O in free stream and the dissociation of free stream O_2 in the shock region. The free stream mole fractions of O and O_2 are decreasing and increasing respectively with decreasing altitude as shown in Tab. 3.3. Because of this contrasting trend, although a steady increase of the mole fraction of NO is observed with decrease in altitude for our range of 100 to 200 km, a general comment cannot be made for NO mole fractions produced in the shock regions of the flow at other altitudes. Figure 5.1 shows the surface flux of particles striking the stagnation point of the CubeSat for different altitudes, and it is more evident from these curves that the concentration of NO is increasing, but is never higher than that of O. Figure 5.1 also shows that at higher altitudes where formation of NO is less likely, sensitivity to modeling parameters also becomes weaker.

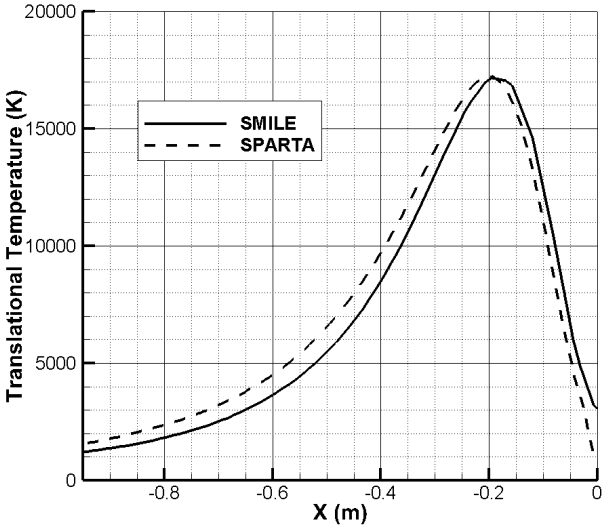

(a) Stagnation line translational temperature profile for two different DSMC codes.

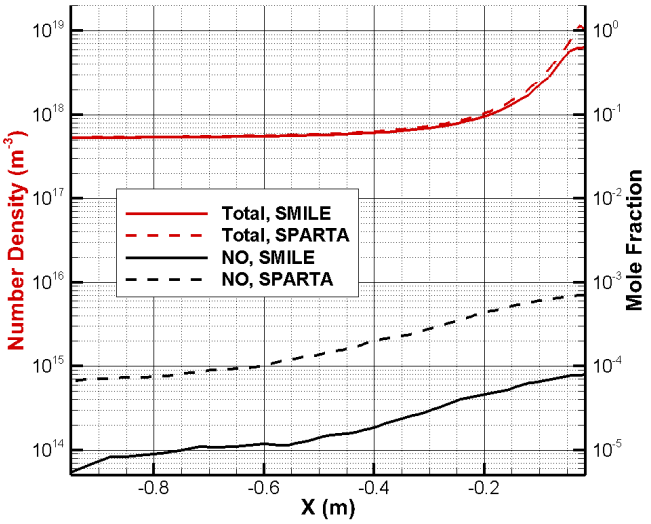

(b) Stagnation line total number density and mole fraction of NO for two different DSMC codes.

Figure 4.6: Comparison of stagnation streamline macro parameters for Cases 2(a) and 2(b).

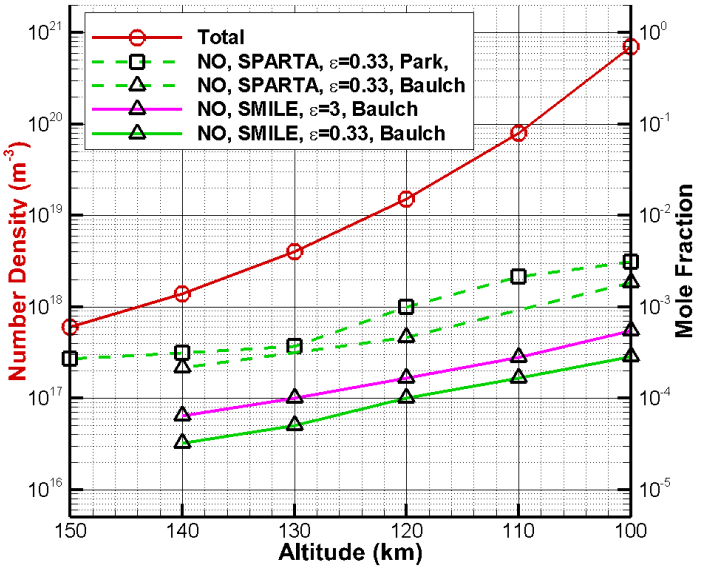

Figure 4.7: Stagnation point total number density of all species with change in altitude (red). Stagnation point mole fractions for NO is shown for different chemical reaction rates (symbols), DSMC code (line style), and different CubeSat orientation (color).

Chapter 5

Radiation Estimates

5.1 Visible Radiation

A spectrometer onboard CubeSat will be dedicated to the radiation in the spectral range from 500 to 800 nm. As mentioned before, NO_2^* is the prime source of emission spectra in the visible spectral range. and since it is a tri-atomic molecule, its spectra is broad ranging from 500 to 800 nm [27, 28]. Surface flux data using the SPARTA code, shown in Fig. 5.1, is used to calculate the radiance (in Rayleighs) for NO_2^* given by Eq. 3.7. In Fig. 5.2(a), the radiance is slightly higher for the $\epsilon = 3.0$ orientation of CubeSat compared to $\epsilon = 0.33$ orientation because of the larger NO flux on the surface, as discussed in Fig. 5.1. Although the gas phase calculations using the chemistry model of Park [10] generate more NO compared to Baulch [12], the NO mole fraction near the surface does not show a significant difference, as was shown in Fig. 4.7. This is reflected in Fig. 5.2(a) where the radiance due to the Park and Baulch rates for $\epsilon = 0.33$ are nearly the same. Figure 5.2(a) also compares the NO_2^* radiance prediction from Gimelshein et al.[7] for a cylindrical geometry of the Atmospheric Explorer (AE) (diameter= 2 m). Since our geometry is more than one order of magnitude smaller in comparison, the radiance for the CubeSat is about an order of magnitude smaller than that of AE, which can be seen in Fig. 5.2(b).

5.2 UV Radiation

Onboard the CubeSat, two spectrometers will measure UV radiation that is produced from gas-phase molecules undergoing electronic transitions in the wavelength range from 205 to 255 nm. Figure 5.3 shows the NO(γ) and NO(β) band emission profiles. At the altitude of 100 km, the NO(β)-band emission is the highest it will be for the altitudes simulated, and is still more than one magnitude lower in intensity than the peak emission from NO(γ)-band emission, so the peak emission of NO(γ)-band is the most important in this work. Similar to Fig. 4.7, Fig. 5.4 demonstrates the sensitivity of NO (γ)-band radiation to different modeling parameters. Inspection of the plot shows that the highest predicted radiance at each altitude

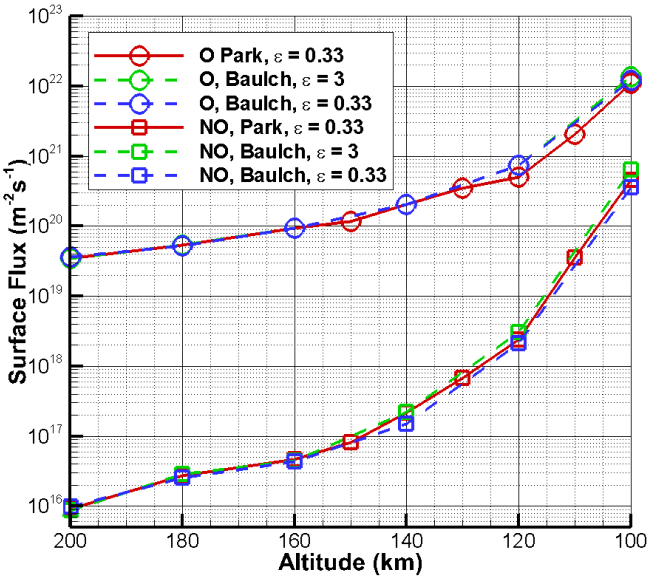

Figure 5.1: Surface flux of NO and O at the stagnation point of the CubeSat for different altitudes using SPARTA.

is from the simulation using the largest aspect ratio using the SPARTA code. This is because, as it was shown in Fig. 4.4, the temperature is elevated along the stagnation, and so is the population of NO. This combination is predicted to have most NO particles and a larger fraction of particles in the (A) state, since the electronic temperature is assumed equal to the translational temperature. Using a smaller aspect ratio with the rates of Park [10] yields the next highest value because even though the temperature profile is not as broad, the population of NO is elevated over NO populations predicted using the rates of Baulch [12]. Figure 5.5 shows the altitude dependence of NO(γ)-band and NO(β)-band emission averaged over 15 Å, the approximate spectral resolution of the onboard spectrometers. It can also be seen in Fig. 5.5 that from 100 to 120 km, the difference between the peak and valleys of the curves increases because of the decrease in NO(β)-band intensity with increasing altitude.

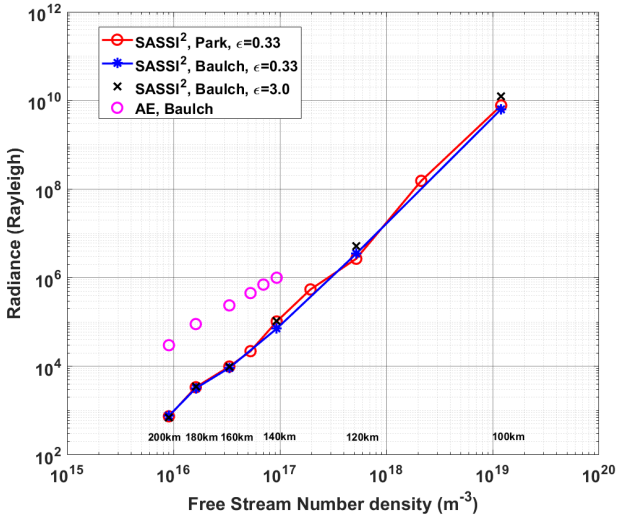

(a) Radiance of NO_2^* emission at different altitudes using rates of Park and Baulch.

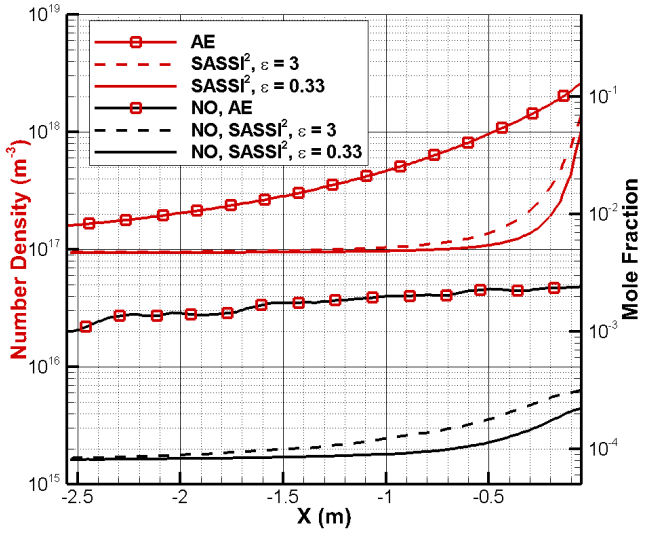

(b) Stagnation line number density for AE and SASSI^2 simulations at 140 km using rates of Baulch.

Figure 5.2: Comparison of NO_2^* emission estimates between AE and SASSI^2 simulations using SPARTA.

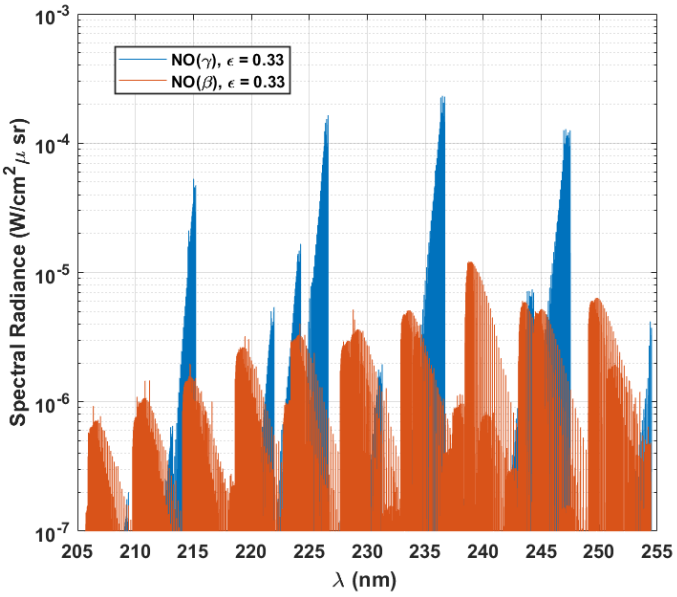

Figure 5.3: Line-by-line spectral radiance of NO(γ)-band and NO(γ)-band emission at 100km using SPARTA, rates of Baulch, and an aspect ratio of $\epsilon = 0.33$. $\Delta\lambda = 6.3 \times 10^{-3}$Å.

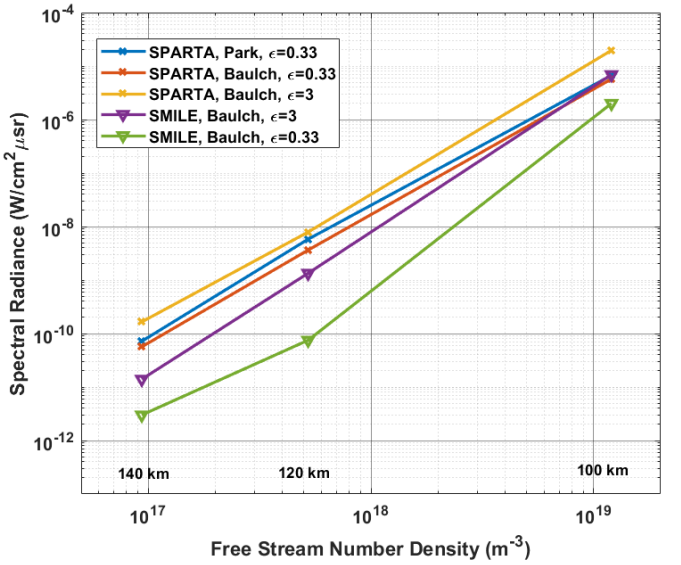

Figure 5.4: Difference in mean radiance of NO (γ)-band emission spectrum over 205 to 255 nm wavelength range, with change in chemical reaction set, DSMC code, and CubeSat aspect ratio ϵ. A pass-band filter for 230 $\pm$ 25nm is used from Levin.

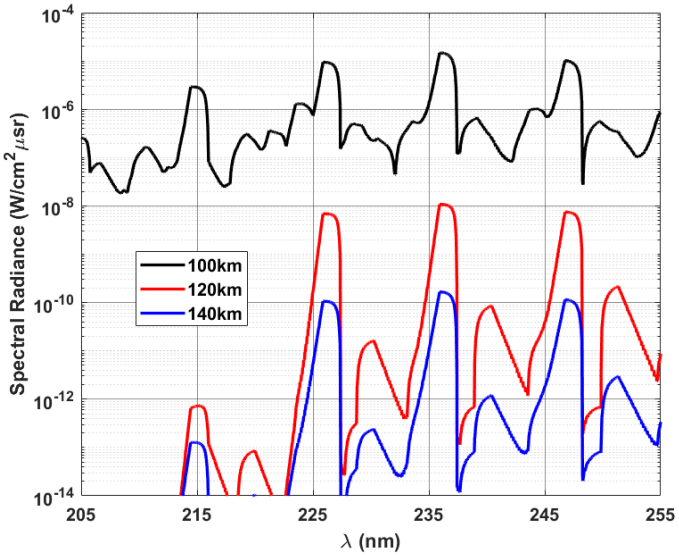

Figure 5.5: NO(γ) and NO(β)-band emission profiles in the 205 to 255 nm wavelength range across 100, 120, and 140km, using SPARTA, rates of Baulch, and an aspect ratio of $\epsilon = 0.33$.

Chapter 6

Conclusions

Numerical calculations have been performed to determine the sensitivity of previous work to dissociation and reverse exchange reactions for NO. It has been found that dissociation and reverse exchange mechanisms have negligible effect on the NO produced during the time the particle resides in the bow shock. DSMC flowfield solutions for altitudes from 100 to 200 km have been performed using the SPARTA and SMILE codes. It has been determined that the calculated probability for the first Zel'dovich reaction to occur by SMILE or SMART has the greatest impact on the prediction of NO formation in the diffuse shock region of the 3U CubeSat. Estimates of NO formation have been used to determine the amount of NO_2 that will be present due to surface reactions, and the tangent slab approximation has been used to estimate the spacecraft glow radiance in the visible range. After selecting mechanisms for electronic state excitation, calculations using NEQAIR have shown the intensity of radiation that can be expected from NO and it has been determined that the NO(γ)-band radiation is the most significant band of ultraviolet radiation for this mission. A comparison with simulations performed at similar altitudes for previous missions has shown that the radiation intensity is strongly dependent on the size of the geometry, which directly influences the size of the shock interaction region.

References

[1] Park, C., "Nonequilibrium Hypersonic Aerothermodynamics," 1989.

[2] Bird, G., "Molecular Gas Dynamics and the Direct Simulation Monte Carlo of Gas Flows," *Clarendon, Oxford*, Vol. 508, 1994, pp. 128.

[3] Park, C., "Nonequilibrium Air Radiation (NEQAIR) Program [Microform]: User's Manual/Chul Park," *NASA, TM-86707*, 1985.

[4] Cauchon, D. L., "Radiative Heating Results from the FIRE II Flight Experiment at a Reentry Velocity of 11.4 Kilometers per Second," *NASA TM X-1402*, Vol. 6, 1967.

[5] Levin, D., Candler, G., Collins, R., Erdman, P., Zipf, E., Espy, P., and Howlett, C., "Comparison of Theory with Experiment for the Bow Shock Ultraviolet Rocket Flight." *Journal of Thermophysics and Heat Transfer*, Vol. 7, No. 1, 1993, pp. 30–36.

[6] Levin, D. A., Candler, G. V., Collins, R. J., Erdman, P. W., Zipf, E. C., and Howlett, L. C., "Examination of Theory for Bow Shock Ultraviolet Rocket Experiments-I," *Journal of Thermophysics and Heat transfer*, Vol. 8, No. 3, 1994, pp. 447–452.

[7] Gimelshein, S., Levin, D., and Collins, R., "Modeling of Glow Radiation in the Rarefied Flow About an Orbiting Spacecraft," *Journal of Thermophysics and Heat transfer*, Vol. 14, No. 4, 2000, pp. 471–479.

[8] Dogra, V. K., Collins, R. J., and Levin, D. A., "Modeling of Spacecraft Rarefied Environments Using a Proposed Surface Model," *AIAA Journal*, Vol. 37, No. 4, 1999, pp. 443–452.

[9] Morgan, J., Nuwal, N., Williams, J., Putnam, Z. R., Levin, D., Pikus, A., Berger, A., and Alexeenko, A., "Prediction of Flight Measurements of High-Enthalpy Nonequilibrium Flow from a CubeSat-Class Atmospheric Probe," *AIAA Aerospace Sciences Meeting*, Vol. 812, 2018.

[10] Li, Z., Sohn, I., and Levin, D. A., "Modeling of Nitrogen Monoxide Formation and Radiation in Nonequilibrium Hypersonic Flows," *Journal of Thermophysics and Heat Transfer*, Vol. 28, No. 3, 2014, pp. 365–380.

[11] Park, C., "Review of Chemical-Kinetic Problems of Future NASA Missions. I-Earth Entries," *Journal of Thermophysics and Heat transfer*, Vol. 7, No. 3, 1993, pp. 385–398.

[12] Baulch, D. L., "Evaluated Kinetic Data for High Temperature Reactions," *Cleveland, CRC Press [1972-*, 1972.

[13] Luo, H., Kulakhmetov, M., and Alexeenko, A., "Ab initio state-specific N 2 + O Dissociation and Exchange Modeling for Molecular Simulations," *The Journal of Chemical Physics*, Vol. 146, No. 146, 2017, pp. 24309–24310.

[14] Cruden, B. A. and Brandis, A. M., "Measurement of Radiative Non-equilibrium for Air Shocks Between 7-9 km/s," *47th AIAA Thermophysics Conference*, 2017, p. 4535.

[15] Andrienko, D. and Boyd, I. D., "State-resolved Characterization of Nitric Oxide Formation in Shock Flows," *2018 AIAA Aerospace Sciences Meeting*, 2018, p. 1233.

[16] Dikalyuk, A., Kozlov, P., Romanenko, Y., Shatalov, O., and Surzhikov, S., "Nonequilibrium spectral radiation behind the shock waves in Martian and Earth atmospheres," *44th AIAA Thermophysics Conference*, 2013, p. 2505.

[17] Bose, D. and Candler, G. V., "Thermal Rate Constants of the N_2+ O→ NO+ N Reaction using ab initio 3A" and 3A' Potential Energy Surfaces," *The Journal of chemical physics*, Vol. 104, No. 8, 1996, pp. 2825–2833.

[18] Gallis, M. A., Torczynski, J. R., Plimpton, S. J., Rader, D. J., and Koehler, T., "Direct simulation Monte Carlo: The quest for speed," *AIP Conference Proceedings*, Vol. 1628, 2014, pp. 27–36.

[19] Ivanov, M., Kashkovsky, A., Gimelshein, S., Markelov, G., Alexeenko, A., Bondar, Y. A., Zhukova, G., Nikiforov, S., and Vaschenkov, P., "SMILE System for 2D/3D DSMC Computations," *Proceedings of 25th International Symposium on Rarefied Gas Dynamics, St. Petersburg, Russia*, 2006, pp. 21–28.

[20] Jacchia, L. G., "Thermospheric Temperature, Density, and Composition: New Models," *SAO Special Report*, Vol. 375, 1977.

[21] McCoy, R. P., "Thermospheric Odd Nitrogen: 1. NO, N (4 S), and O (^{3}P) Densities from Rocket Measurements of the NO δ and γ Bands and the O2 Herzberg I Bands," *Journal of Geophysical Research: Space Physics*, Vol. 88, No. A4, 1983, pp. 3197–3205.

[22] Jelezniak, M. and Jelezniak, I., "CHEMKED 3.3," 2013.

[23] Zuiker, N. J., Williams, J., Putnam, Z. R., Levin, D. A., Ghosh, A., Goggin, M., and Alexeenko, A., "Design of a CubeSat Mission to Investigate High-Enthalpy Nonequilibrium Flow Chemistry," *2018 AIAA Aerospace Sciences Meeting*, 2018, p. 1936.

[24] Gasser, R. P. H. and Ehrlich, G., "An Introduction to Chemisorption and Catalysis by Metals," *Physics Today*, Vol. 40, 1987, pp. 128.

[25] Murad, E., "The Shuttle Glow Phenomenon," *Annual Review of Physical Chemistry*, Vol. 49, No. 1, 1998, pp. 73–98.

[26] Erdman, P. W., Zipf, E. C., Espy, P., Howlett, L. C., Levin, D. A., Collins, R. J., and Candler, G. V., "Measurements of Ultraviolet Radiation from a 5-km/s Bow Shock," *Journal of Thermophysics and Heat Transfer*, Vol. 8, No. 3, 1994, pp. 441–446.

[27] Karipides, D. P., Boyd, I. D., and Caledonia, G. E., "Detailed Simulation of Surface Chemistry Leading to Spacecraft Glow," *Journal of Spacecraft and Rockets*, Vol. 36, No. 4, 1999, pp. 566–572.

[28] Kenner, R. and Ogryzlo, E., "Orange Chemiluminescence from NO2," *The Journal of chemical physics*, Vol. 80, No. 1, 1984, pp. 1–6.